Dislocation mechanisms in the first stage of plasticity of nanoindented Au(111) surfaces

A. Asenjo* and M. Jaafar
Instituto de Ciencia de Materiales-CSIC, Campus de Cantoblanco 28049 Madrid, Spain

E. Carrasco and J. M. Rojo
Departamento de Física de Materiales, Universidad Complutense, 28040 Madrid, Spain
(Received 28 July 2005; revised manuscript received 29 November 2005; published 27 February 2006)

The onset of plasticity in Au(111) has been analyzed at the atomic scale. Images of dislocation traces and other features obtained by atomic force microscopy around nanoindentations have been correlated with force vs penetration curves obtained in the same experiment. It has been demonstrated that the discontinuities in force vs penetration curves are associated to the generation and glide of dislocation loops with well-characterized parameters. Half loops intersecting the surface, with screw components, are recognized and processes of cross-slip identified. The formation of terraces and permanent traces around the nanoindentation points has been explained in terms of the elastic theory of dislocations in a continuum.

DOI: 10.1103/PhysRevB.73.075431 PACS number(s): 61.72.Bb, 61.72.Ff, 68.55.Ln, 68.35.Gy

I. INTRODUCTION

In the last few years, nanoindentation has been developed as a way of obtaining information about local mechanical properties of solid surfaces.[1–9] Nanoindentation is distinguished from the time-honored technique of microindentation in that the contact with the surface under analysis is made by a tip of nanometer dimensions, which, under favorable circumstances, can also be employed to obtain images of the surface at the nanolevel. In the course of nanoindentation, several groups[4–7] have identified discontinuities in the stress-strain curves (sometimes called the "pop-in" effect), which have been ascribed to the generation of dislocations. These discontinuities appear at stresses that are consistent with the theoretical estimate of the minimum stress needed to make compact planes to glide on each other, the so-called ideal critical shear stress. However, the mechanisms by which dislocations are individually emitted, the characteristic parameters of those dislocations and their individual relationship to the discontinuities in the force vs penetration curves are, to a large extent, still unknown. Much uncertainty exists, too, about the processes at the atomic level by which matter is carried away from the nanoindentation trace: diffusion is often assumed to play an important role,[10] although other mechanisms are possible, such as the ones discussed in the present paper.

By using scanning tunnel microscopy (STM), some of us have recently described[11] the individual generation of certain dislocation configurations following nanoindentations in Au(001) and been able to identify the parameters (such as Burgers vector, geometry, etc.) of those configurations as well as their evolution under different external conditions.[12] Unfortunately, under the experimental conditions of STM, a measurement of the local forces involved in the dislocation generation is not feasible and a direct correlation between discontinuities in the force vs penetration curves and images of dislocation configurations cannot be attempted. In the present paper we report on that correlation through an analysis carried out with an atomic force microscope (AFM), which is able to provide a direct measurement of the load involved in the nanoindentation while providing an image, albeit at a lower resolution, of the nanoindented site. We have investigated the initial stages of plasticity after nanoindenting an Au(111) surface with successively increasing loads and have succeeded in relating the discontinuities in the force vs penetration curves with the emergence of well-characterized dislocation configurations as well as with local modifications of the metal surface, in particular, the appearance of permanent traces once the tip is removed. All our results have been analyzed in terms of the elastic theory of dislocations in a continuum; in particular, the stresses arising from the nanoindentation have been estimated and compared to the predictions of the different models at the atomic scale.

II. EXPERIMENTAL

The Au samples were prepared by vacuum evaporation onto NaCl substrates. Although the samples had a polycrystalline character, the nanoindentation experiments were carried out in the large (>1 μm) terraces oriented in the (111) direction. The surface, previously annealed until reaching a reddish color under a flame, showed larger than 500 nm terraces. The nanoindentations were made either at ambient conditions or under nitrogen flow (up to 6% humidity) by using a Nanotec Electronica S.L. AFM system. We used silicon cantilevers from nanosensors with a force constant of $k_c \approx 40$ N/m and Si tip radius of $R \approx 10$ nm.

The cantilever deflection Δs was calibrated for every indentation experiment measuring the cantilever displacement vs the z piezoexcursion on a sapphire surface. In order to reduce the errors due to nonlinearity and creep of the piezos, the measurement parameters of these calibration curves are similar to the ones used in the nanoindentation experiments. Assuming the sapphire surface is not deformed, the piezodisplacement corresponds to the cantilever displacement resulting in an effective calibration of the cantilever deflection. In the indentation experiments, the penetration can be evaluated as $\delta = z - \Delta s$ were z is the piezoexcursion. The applied force can be calculated as $F = k_c \Delta s$.

 ©2006 The American Physical Society

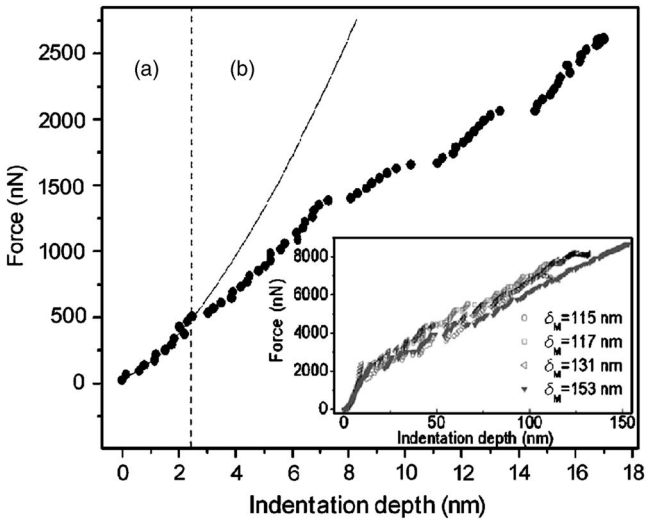

FIG. 1. Force vs penetration curves obtained with an AFM tip of ca. 10 nm radius. Note two distinct regions: (a) small forces leading to reversible behavior with no discontinuities and (b) onset of plasticity, translated into the appearance of discontinuities in the curves. The full line results from the fitting of the elastic region data to a $\delta^{3/2}$ law. The inset corresponds to a series of four F vs δ curves for successively increasing maximum penetration.

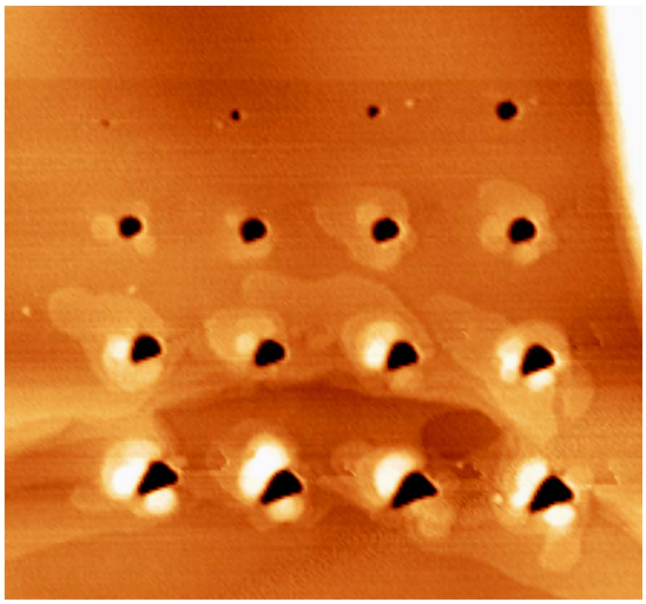

FIG. 2. (Color online) AFM images of 16 nanoindentations obtained after force vs penetration tests as the ones shown in Fig. 1. Note the terraces around the nanoindentation traces. Image size: 2.2 μm$\times$2 μm.

Large terraces were selected to perform the indentation experiments. In order to prevent the lateral forces as well as the lateral displacement of the cantilever, in all the experiments the angle between the cantilever and the sample was kept near to zero.

After the indentation experiments, the topography of the modified region was recorded by AFM. To obtain a value for the maximum depth of every indentation, the profiles across the permanent traces were measured. In addition, the lateral dimensions of a given trace can be determined. Two different methods were used to estimate the indentation area: in the first one, a direct measurement of the image was performed assuming a triangular or elliptical trace shape; in the second case, the flooding method provided by the WSXM Nanotec Electronica S.L. program was applied.[13]

III. RESULTS

A typical curve for the external load F vs indentation depth δ is shown in Fig. 1. Two regions are neatly distinguished. In the region (a) shown in Fig. 1, corresponding to stresses below a certain threshold of approximately F_{thr} =500 nN, no discontinuity in the force vs penetration curve is discernible. Furthermore, in this region the curves are fully reversible and no traces of the nanoindentation are visible in AFM images taken after retrieving the tip. In the region (b) shown in Fig. 1, corresponding to external loads higher than F_{thr} displacement excursions (pop-ins) of different extent are clearly visible. All the nanoindentations in this second region result in permanent traces after retrieving the tip, these traces increasing their diameter as the load increases. Because of that plastic deformation, the load-unload curves show hysteresis effects. The inset in Fig. 1 shows a series of four F vs δ curves in each of which the value of the maximum force (upper load), F_M, is successively increased while keeping it always above F_{thr} [in the region (b) of Fig. 1]. Note the clearly visible discontinuities.

For a series of 16 runs like those of Fig. 1, the AFM images obtained after retrieving of the tip are shown in Fig. 2. The corresponding force vs penetration curves are shown as an inset of Fig. 1. For each value of F_M, the depth t_d of the resulting permanent craters is measured. The results are shown in Table I along with the values of the maximum penetration δ_M for the corresponding upper load. To make a separate check of the consistency of the F vs δ data for each run in Fig. 2, the depth of the permanent trace directly, as measured from a depth profile in the AFM image, has been compared to the sum of the plastic displacements (pop-in excursions) in the F vs δ curves. The results are shown in Fig. 3. Note that both sets of points superimpose on each other within the experimental error (due to the inaccuracies in the piezotube movement and in the calibration of the cantilever deflection). In terms of a simple punch-like mechanism, one would expect that the emission of every single prismatic loop into the bulk would leave behind a permanent trace equal to the excursion of the tip, i.e., the discontinuity segment length. This shows that, under our experimental conditions, partial refilling of the initial hollow craters due to long-range surface diffusion processes is undetectable.

A most important feature is also depicted in Fig. 2: one can identify around the traces well-formed terraces, one interatomic distance high, with sides approximately parallel to the three compact directions in the surface. For loads smaller than the one corresponding to the third trace, these terraces are not visible although their existence, just after the nanoindentation, cannot be discarded; they could be small enough to disappear by tip effects combined with short-range diffu-

TABLE I. I_o is the indentation order; δ_M, maximum penetration; d, sum of discontinuities; F_M, maximum force; and t_d, trace depth.

I_o	δ_M (nm)	d (nm)	F_M (μN)	t_d (nm)
1	7	1	1.1	1
2	18	6	2.3	3
3	27	9	2.8	3
4	36	14	3.4	15
5	45	25	3.4	21
6	51	29	4.3	28
7	53	32	4.7	32
8	66	34	5.3	38
9	80	38	5.1	44
10	88	47	5.7	43
11	100	51	6.2	44
12	98	51	7.1	50
13	115	64	7.1	58
14	117	61	7.8	58
15	131	65	8.2	62
16	153	61	8.7	64

sion. These terraces are compared in Fig. 4 to those imaged by STM around nanoindentations in the Au(001) face.[12] The two types of terraces are very similar; although, of course, their geometry is different. Whereas in the (111) oriented surface, we observe terraces bound by three differently oriented steps, roughly at 120° to each other, we find only two perpendicular ones in the (001) surface. This can be traced back to the geometry of both surfaces: while there are three equivalent ⟨110⟩ directions contained in a {111} surface plane, there are only two in a {001} plane. Note that steps binding terraces in the (111) surface are not so well defined as those in the (001) surface because the former are imaged by AFM in the air and the atmospheric gases tend to round up their edges.

Apart from leaving behind terraces as landmarks of dislocation activity, dislocation generation is also directly observed around the nanoindentation traces. An example is shown in Fig. 5 where the generation and further glide of a

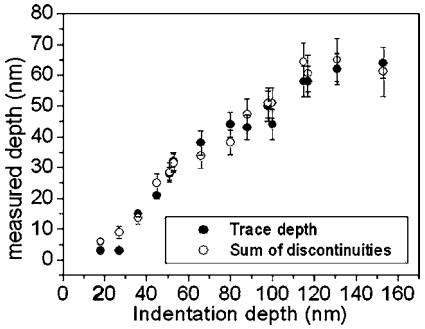

FIG. 3. Comparison of the measured depth of permanent AFM traces and the sum of all the pop-in excursions observed in the F vs δ curves. The data correspond to the indentation series with increasing maximum depth.

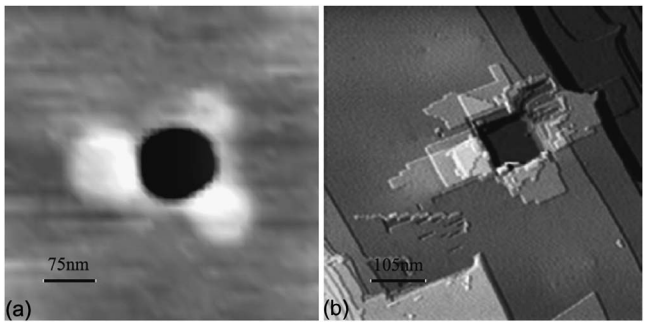

FIG. 4. Permanent nanoindentation traces (a) AFM in air on Au(111) and (b) STM in ultrahigh vacuum on Au(001) (Ref. 12).

screw dislocation can be clearly seen by comparing AFM images of the same area before and after the nanoindentation. Around the nanoindentation point, a permanent hollow crater of hexagonal shape has been created with their three sides parallel to the three compact directions in the (111) face. Near the crater a screw dislocation has been emitted, whose gliding path can be traced from the step it leaves behind; the latter is about one interatomic distance high. Note the sudden

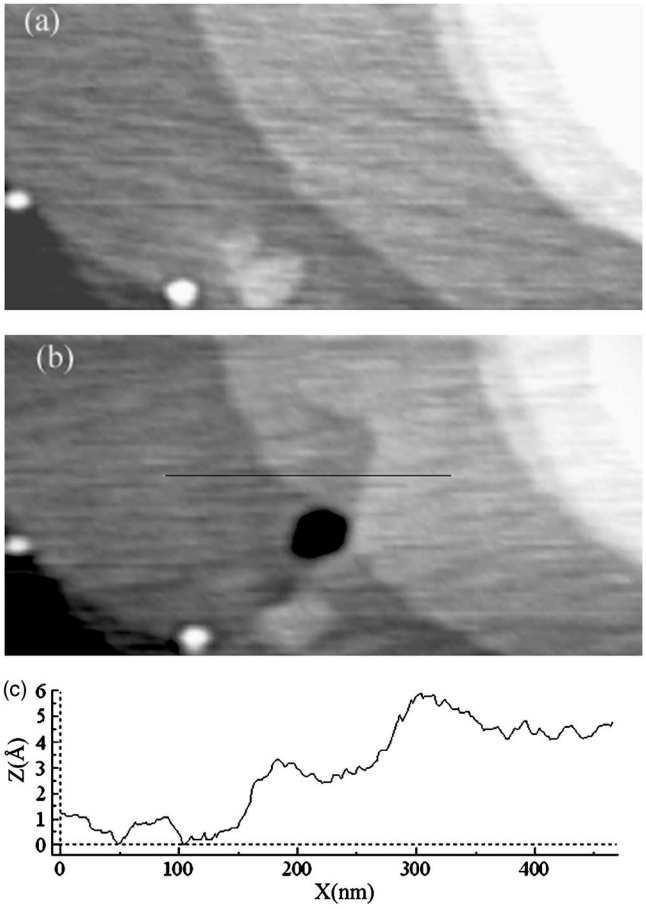

FIG. 5. AFM image of the same area (a) before and (b) after the nanoindentation (see the black permanent trace), along with the corresponding depth profile of the latter (c), showing the generation and further glide of a screw dislocation. Note the step created at the trail of the dislocation and the revolving depth trace around the final position of the dislocation. Image size: 1 μm $\times$ 0.5 μm.

change in the direction of the path, accountable in terms of cross-slip.

To obtain an estimation of the threshold stress required to reach the first discontinuity in the force vs penetration curve, we compute the stress distribution in the sample at the neighborhood of the nanoindentation. Assuming a hemispherically ended AFM tip, the well-known model of Hertz can be used. For an external load F, if R is the radius of the tip, the radius of the Hertz contact circle a_H and the penetration depth δ can be written as a function of the effective Young modulus $\bar{E}$[14] as follows:

$$a_H = \left(\frac{3FR}{4\bar{E}}\right)^{1/3},$$

$$\delta = \left(\frac{9F^2}{16R\bar{E}^2}\right)^{1/3}. \tag{1}$$

According to the Hertz theory, the distribution of compressions across the points $(x'y')$ distant $r' = \sqrt{x'^2 + y'^2}$ from the center of the Hertzian circle of contact is known to be

$$p(r') = p_0\left(1 - \frac{r'^2}{a_H^2}\right)^{1/2} \quad \text{where } p_0 = \frac{3F}{2\pi a_H^2}. \tag{2}$$

Now, the calculation of stresses in the bulk of the nanoindented material is reduced to the problem of an elastically deformed semi-infinite medium limited by a plane and subjected to an external stress given by (2). As is well known,[15] the displacements in a generic point $r=(x,y,z)$ in the bulk can be written in terms of the elastic Green tensor $G(r-r')$ as

$$u_i(r) = \sum_j \int\int_{r<a_H} G_{ij}(r-r')p_j(r')dx'dy', \tag{3}$$

where $i,j=x,y,z$.

Assuming the external pressure p has only components parallel to z, $p_x(r')=p_y(r')=0$, (3) reduces to

$$u_i(r) = \int\int_{r<a_H} G_{iz}(r-r')p_z(r')dx'dy'. \tag{4}$$

For our geometry, in which the load is applied parallel to the z direction, the explicit form of the Green tensor components in terms of the elastic Lamé constants, λ and μ, and of the modulus of $s=|r-r'|$ is given by[15]

$$G_{xz}(r-r') = \Lambda\left(\frac{(x-x')z}{s^3} - \frac{\mu}{\mu+\lambda}\frac{(x-x')}{(z+s)s}\right),$$

$$G_{yz}(r-r') = \Lambda\left(\frac{(y-y')z}{s^3} - \frac{\mu}{\mu+\lambda}\frac{(y-y')}{(z+s)s}\right),$$

$$G_{zz}(r-r') = \Lambda\left(\frac{z^2}{s^3} + \frac{2\mu+\lambda}{\mu+\lambda}\frac{1}{s}\right),$$

$$\Lambda = \frac{1}{4\pi\mu}. \tag{5}$$

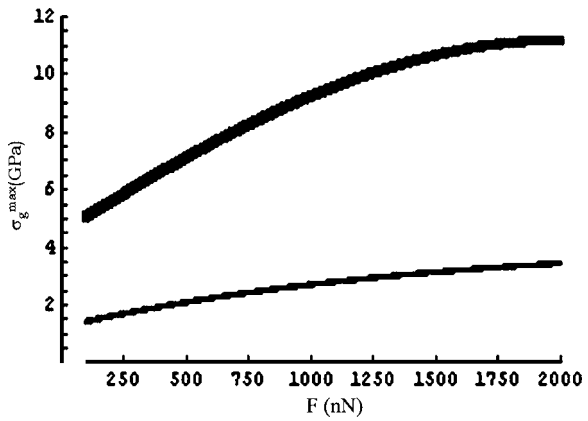

FIG. 6. Computed maximum shear stress $\sigma_g^{\max}$ as a function of the load F. A Hertzian model is assumed. The thick line corresponds to an effective Young's modulus of $\bar{E}=57$ GPa, whereas the thin line corresponds to $\bar{E}=31$ GPa (see text).

Both the strain e_{ij} and stress σ_{ij} tensors can be immediately written by just deriving Eqs. (5) and using Hooke's law[15]

$$e_{ij} = \frac{1}{2}\left(\frac{\partial u_i}{\partial x_j} + \frac{\partial u_j}{\partial x_i}\right),$$

$$\sigma_{ij} = \lambda e_{kk}\delta_{ij} + 2\mu e_{ij}. \tag{6}$$

Equations (1)–(6) can be easily programed in a personal computer and the results σ_{ij} obtained for the different points in the bulk. From the value of σ_{ij}, one can compute the force per unit area on a given lattice glide plane and then project that force along a given glide direction—the equivalent to a local Schmidt's law procedure. Taking the inward normal to the sample as [111], we have done that operation for the easy-glide $(11\bar{1})$ plane and for the easy-glide $\langle 011\rangle$ direction and obtained in such a way a resultant glide-force per unit area $\sigma_g(r)$ for each bulk point.

For each value of the external load F, there is a point (x,y,z) in the bulk in which the glide force σ_g is a maximum $\sigma_g^{\max}$, which is, in fact, the maximum stress available to initiate slip in the crystal. The depth corresponding to $\sigma_g^{\max}$ is found to increase with the external load, its value being close to $a_H/2$.

In Fig. 6, we show the values of $\sigma_g^{\max}$ as a function of F, for reasons discussed later we present two curves corresponding to $\bar{E}=57$ GPa (thick line) and to $\bar{E}=31$ GPa (thin line).

There is little doubt that the region (a) of the curve of Fig. 1 corresponds to the elastic part of the deformation curve. Using Eq. (1) one gets the well-known result that $F \propto \delta^{3/2}$ with a prefactor $p=\frac{4}{3}\bar{E}R^{1/2}$. The points in Fig. 1(a) fit reasonably well to that exponential law with an experimental prefactor of $p=130$ GPa nm$^{1/2}$. If we take for the radius a value of $R=10$ nm, as given by the manufacturer, we end up with a value of $\bar{E}=31$ GPa (note that here $\bar{E}\approx E_{\mathrm{Au}}$), definitely smaller than the bulk value for Au. On the other hand, if we use the bulk value of $E_{\mathrm{Au}}=80$ GPa, the radius would have to

be ~3 nm—a value much too low to be credible. There are suggestions in the literature[5,16] that the Young's modulus of a metal can be lower near the surface of a thin film, a value of $E_{Au}=50$ GPa having been reported recently.[16] It is likely that a combination of this factor with a value of R lower than the nominal one could account for our observations. On these grounds, to construct the curves of Fig. 6, we have taken an upper bound of $\bar{E}=57$ GPa and a lower bound of $\bar{E}=31$ GPa.

We analyze now the plastic stage. As shown in Sec. II, our results show there is a correlation between discontinuities in the load vs penetration curve and the emergence of permanent traces in the AFM image once the tip is removed. These features (as seen in Fig. 2) are craters and terrace steps both with crystallographically oriented sides. This strongly suggests that a mechanism involving dislocation glide underlies permanent trace formation and that diffusion, either intrinsic in the surface or induced by the tip, is not the prevailing mechanism.

Terrace steps winding around the crater traces of nanoindentations have been previously interpreted[11,12] in terms of cross-slip of *screw loops*. The latter are, in fact, half loops of which, at least, one of the segments intersecting the (111) surface is in a screw orientation, e.g., [110]. This segment can, of course, glide on a plane, leaving behind a step parallel to the projection of the glide direction. Our present results support that interpretation: in our case, as can be realized by comparing Figs. 4(a) and 4(b), we have a different geometry with a [111] surface normal with three easy-glide {111} equally inclined planes with respect to the surface normal. Screw dislocations gliding on these planes, along ⟨110⟩ directions, would result in three types of terraces at 120° to each other. Whereas the direction of the sides of terraces are restricted to the above directions, depending on the orientation and position of the original dislocation segments, one can obtain terraces with different shapes, resulting from a combination of piecewise straight segments of dislocation. An example of a possible geometry is depicted in Fig. 7, where the two screw segments of the original loop intersecting the surface are assumed to be parallel and there are multiple processes of cross-slip as described in the figure caption. Note that, in general, the terraces may or may not close. It is to be remarked that out of the three skewed {111} planes, only the two planes that intersect along the screw segment direction are operative in the glide process.

We can also understand the formation of craters with crystallographically oriented sides in terms of a similar mechanism of cross-slip. Indeed, a sequence of successive processes of loop creation and terrace winding can result in a permanent trace in the shape of a crater with sides parallel to the intersection of the surface with the gliding planes, in our case the ⟨110⟩ directions contained in the (111) surface plane. The shape of the crater is then a polygon with sides parallel to the compact directions in the surface (111) plane; it can be a triangle, a hexagon, or have even a more complex shape. An example of an experimental hexagonal trace can be seen in Fig. 5. Note that in the case of a surface with a [001] normal, rectangular traces would be expected instead, as can be seen by comparing the traces of Figs. 4(a) and 4(b). The

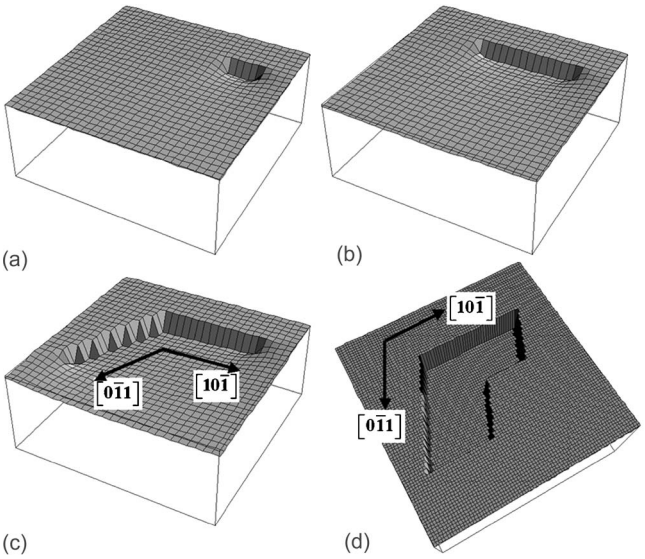

FIG. 7. A scheme of the initial geometry and a possible closed trajectory of a screw loop on a (111) surface. (a) An initial screw loop with Burgers vector $\mathbf{b}=a/2\ [110]$ is generated on a $(1\bar{1}1)$ plane, the corresponding surface step running along the $[10\bar{1}]$ direction. (b) One of the two screw segments of the loop glides along $[0\bar{1}1]$ on the loop plane. (c) This segment cross-slips onto a $(1\bar{1}\bar{1})$ plane, the trailing step making a sharp turn of $2\pi/3$. (d) The segment makes a succession of cross-slips canceling at the end of its trail the other initial screw segment (seen from a different perspective). The final configuration consists of a closed terrace on the surface and a prismatic loop of Burgers vector **b** in the bulk.

signature of the terrace steps left behind by the glide of the screw loops that we propose agree with mechanisms proposed earlier by other groups[17] to account for the dislodgement of matter and subsequent pileup around a nanoindentation, including the possible role of cross-slip.[7]

For an external load exceeding that giving rise to plasticity landmarks, i.e., discontinuities in the load vs penetration curves, craters are always present. One should remark that beyond that plasticity threshold, winding terraces are also visible except for nanoindentations corresponding to the lowest loads (the three first nanoindentations of Fig. 3). We suspect, however, that in these cases the terraces might be too small to be disclosed in the corresponding images. The data strongly suggest that, once the dislocations are created, further dislocation activity, in the form of cross-slip, always takes place, giving rise to both terraces and craters. It is also worth remarking that cross-slip provides a mechanism for redistributing matter around the nanoindentation other than the usually assumed of surface diffusion.

We analyze now, quantitatively, the stresses involved in the onset of plasticity. The first discontinuity in the load vs penetration curve of Fig. 1 corresponds to a threshold of $F_{thr}=500$ nN. It is interesting to remark that simulations carried out with a realistic large crystal of Au[18] [albeit with an (001) orientation] yield a first discontinuity of the same order, at ~800 nN. From the value of F_{thr}, using the results shown in Fig. 6 we obtain an experimental value for the threshold stress capable of generating dislocations (the criti-

cal shear stress) in the interval $2 < \sigma_g^{\max} < 6.5$ GPa.

The theoretical ideal value of the critical shear stress, i.e., the minimum stress needed to make compact planes to glide on each other, is estimated in textbooks[19] as $\sigma_{\text{theo}} \approx \mu/2\pi$, which for Au is equal to 4.3 GPa. Although that estimation is based on a very simple model, the more elaborate calculations[6] do not change appreciably this value. The value that we have obtained for $\sigma_g^{\max}$ through a Hertzian analysis of our experimental data is in the interval 2–6.5 GPa, whose order of magnitude is consistent with the theoretical value of σ_{theo}. The above interval can be also compared to previous determinations of the resolved shear stress in Au by Kiely and Houston,[4] 1.7 GPa, and Corcoran *et al.*,[2] 3.0 GPa, and in Al by Van Vliet *et al.*,[5] 3.4 GPa, although the radii of the tips in those experiments were almost an order of magnitude higher than ours. If we identify the onset of plasticity with the appearance of the first discontinuity in the load vs penetration curve and the disappearance of reversibility, we have to conclude that the yield stress around a nanoindentation is of the order of the theoretical ideal value of the critical shear stress. In search of an explanation for this different behavior of the surface and the bulk, we argue that, in nanoindentation tests, only a relatively small volume of the crystal participates in the process and it is most probable that this volume is free of preexisting dislocations. The fact that plasticity around a nanoindentation starts at loads comparable to the ones required to generate dislocations in an ideal defect-free crystal has been recognized in earlier work by other groups, although in most cases[2,5–7] both the tip radius and the loads used have been at least one order of magnitude larger than in our case, sometimes in the borderline between micro- and nanoindentation.

The above discussion implies that in nanoindented Au(111) surfaces the appearance of permanent deep traces around the nanoindentation center, and of shallow winding terraces around it, take place when shear stresses along the slip direction reach a value of the order of the theoretical shear strength. The underlying mechanism involves generating dislocation loops with a partial screw character, which cross-slip between the different {111} planes thereafter. As we have also shown that nanoindentation traces and terraces are directly associated with discontinuities in the load vs penetration curves, we can safely conclude that there is also a direct relationship between the generation of these loops and the beginning of plasticity around nanoindentations. Needless to say, the above discussion does not preclude the generation of other types of dislocation loops, such as the half loops in the shape of "mesas" described earlier[11] or even those that may glide into bulk and are invisible by surface techniques.

IV. CONCLUSIONS

It is concluded that in nanoindented Au(111) crystals, the onset of plasticity—characterized by the appearance of discontinuities in the load vs penetration curves and the corresponding appearance of hysteretical effects in the latter—is connected with the creation and further movement of a certain class of dislocation loops. Some of these are, in fact, half loops with some of their segments in a screw orientation, gliding parallel to the compact directions in the surface. The nature of the loops is easily recognizable because they give rise to terraces winding around the nanoindentation trace by cross-slip, similar by nature but of a different shape of those reported earlier in (001) faces. We have shown that the generation of these loops takes place when the glide force per unit area in the direction of plane glide is of the order of the critical shear stress for an ideal crystal. The permanent traces of the nanoindentations, which remain after the tip is retracted, are shown to be created by a dislocation mechanism involving the cross-slip of those screw loops and not by simple diffusion and adhesion processes. All those results also point out to an efficient mechanism of mass transport away from the nanoindentation based on dislocation generation and further glide.

ACKNOWLEDGMENTS

This research was performed under the terms of the project No. MAT2003-08627-C02 funding by MCYT that we gratefully acknowledge. A.A. and M.J. acknowledge support from the Comunidad Autonoma de Madrid through project Grant No. GR/MAT/0437/2004.

*Electronic address: aasenjo@icmm.csic.es

[1] U. Landman, W. D. Luetke, N. A. Burnham, and R. J. Colton, Science **248**, 454 (1990).

[2] S. G. Corcoran, R. J. Colton, E. T. Lilleodden, and W. W. Gerberich, Phys. Rev. B **55**, R16057 (1997).

[3] J. Fraxedas, S. Garca-Manyes, P. Gorostiza, and F. Sanz, Proc. Natl. Acad. Sci. U.S.A. **99**, 5228 (2002).

[4] J. D. Kiely and J. E. Houston, Phys. Rev. B **57**, 12588 (1998).

[5] J. Li, K. J. Van Vliet, T. Zhu, S. Yip, and S. Suresh, Nature (London) **418**, 307 (2002); K. J. Van Vliet, J. Li, T. Zhu, S. Yip, and S. Suresh, Phys. Rev. B **67**, 104105 (2003).

[6] D. Lorenz, A. Zeckzer, U. Hilpert, P. Grau, H. Johansen, and H. S. Leipner, Phys. Rev. B **67**, 172101 (2003).

[7] R. Smith, D. Christopher, S. D. Kenny, A. Richter, and B. Wolf, Phys. Rev. B **67**, 245405 (2003).

[8] A. Gannepalli and S. K. Mallapragada, Phys. Rev. B **66**, 104103 (2002).

[9] D. Christopher, R. Smith, and A. Richter, Nanotechnology **12**, 372 (2004).

[10] Diffusion mechanisms are often combined with more complex phenomena arising from the formation of necks when the tip is retracted. See, e.g., Ref. 1.

[11] O. Rodríguez de la Fuente, J. A. Zimmerman, M. A. González, J. de la Figuera, J. C. Hamilton, W. W. Pai, and J. M. Rojo, Phys. Rev. Lett. **88**, 036101 (2002).

[12] E. Carrasco, O. Rodríguez de la Fuente, M. A. González, and J.

M. Rojo, Phys. Rev. B **68**, 180102(R) (2003); E. Carrasco, M. A. González, O. Rodríguez de la Fuente, and J. M. Rojo, Surf. Sci. **572**, 467 (2004).

[13] The flooding method consists of the evaluation of the lake area obtained when the holes are flooded up to certain height. Details in http://www.nanotec.es

[14] K. L. Johnson, *Contact Mechanics* (Cambridge University Press, Cambridge, England, 1985), p. 90.

[15] L. D. Landau and E. M. Lifshitz, *Theory of Elasticity* (Pergamon, New York, 1959), p. 29.

[16] B. Kracke and B. Damascchke, Appl. Phys. Lett. **77**, 361 (2000).

[17] Y. Wang, D. Raabe, C. Klber, and F. Roters, Acta Mater. **52**, 2229 (2004).

[18] J. Knap and M. Ortiz, Phys. Rev. Lett. **90**, 226102 (2003).

[19] C. Kittel, *Introduction to Solid State Physics*, 3rd ed. (Wiley, New York, 1971), p. 672.